

# Thermal Transport in Suspended and Supported Few-Layer Graphene

Ziqian Wang,<sup>†,⊥</sup> Rongguo Xie,<sup>†,‡,§,⊥</sup> Cong Tinh Bui,<sup>||</sup> Dan Liu,<sup>||</sup> Xiaoxi Ni,<sup>‡,§</sup> Baowen Li<sup>\*,‡,§,||</sup> and John T. L. Thong<sup>\*,‡,||</sup>

<sup>†</sup>Department of Electrical and Computer Engineering, National University of Singapore, Singapore 117576, Republic of Singapore, <sup>‡</sup>Department of Physics, National University of Singapore, Singapore 117542, Republic of Singapore, and <sup>§</sup>Centre for Computational Science and Engineering (CCSE) and <sup>||</sup>NUS Graduate School for Integrative Sciences and Engineering, National University of Singapore, Singapore 117456, Republic of Singapore

**ABSTRACT** We report thermal conductivity ( $\kappa$ ) measurements from 77 to 350 K on both suspended and supported few-layer graphene using a thermal-bridge configuration. The room temperature value of  $\kappa$  is comparable to that of bulk graphite for the largest flake, but reduces significantly for smaller flakes. The presence of a substrate lowers the value of  $\kappa$ , but the effect diminishes for the thermal transport in the top layers away from the substrate. For the suspended sample, the temperature dependence of  $\kappa$  follows a power law with an exponent of  $1.4 \pm 0.1$ , suggesting that the flexural phonon modes contribute significantly to the thermal transport of the suspended graphene. The measured values of  $\kappa$  are generally lower than those from theoretical studies. We attribute this deviation to the phonon-boundary scattering at the graphene-contact interfaces, which is shown to significantly reduce the apparent measured thermal conductance of graphene.

**KEYWORDS** Thermal conductivity, graphene, phonon transport, thermal boundary resistance

Graphene has garnered great interest due to its many remarkable physical properties. Its superior room temperature carrier mobility, the possibility of band-gap opening through lateral quantum confinement, and prospects for large-area epitaxial growth makes graphene a promising material for future electronics.<sup>1</sup> In addition, due to the lightweight constituent carbon atoms and the superior crystallinity of its lattice, graphene is believed to have very high thermal conductivity ( $\kappa$ ) near room temperature<sup>2–4</sup> and can thus be used for thermal management in electronic devices. Despite numerous interesting theoretical predictions, few experimental studies<sup>5–9</sup> have been reported on the thermal properties of graphene. Recently the room temperature  $\kappa$  of suspended single-layer graphene (SLG) has been measured with a micro-Raman technique; however reported data show wide variations with values ranging from 600 to 5000 Wm<sup>−1</sup> K<sup>−1</sup>.<sup>5,6</sup> As this technique is normally applied under ambient conditions, the accuracy in estimating  $\kappa$  is not only limited by various assumptions about the laser power absorbed, but also by unknown convective heat losses. By comparison, the conventional thermal-bridge setup offers direct measurements of the heating power and precise temperature ( $T$ ) readout in vacuum, from which  $\kappa$  can be conveniently and accurately extracted. While this technique has been used to study the thermal transport of

supported graphene,<sup>9</sup> the method reported is not applicable to suspended samples.

In this paper, we report thermal conductivity measurements from 77 to 350 K on both suspended and supported few-layer graphene (FLG) using a suspended microelectro-thermal system (METS) in vacuum. We show that  $\kappa$  depends strongly on the graphene size and is lowered in the presence of a substrate. The  $\kappa(T)$  obtained for suspended graphene has a much higher turnover temperature than bulk graphite. The temperature dependence of  $\kappa$  follows a power law with an exponent of  $1.4 \pm 0.1$ , suggesting that the flexural phonon modes contribute significantly to the thermal transport of the suspended graphene. The measured values of  $\kappa$  are generally lower than those from theoretical studies. We attribute this deviation to the phonon-boundary scattering at the graphene-contact interfaces, which will be shown to significantly reduce the apparent measured thermal conductance of graphene.

The METS devices were fabricated following a process similar to that described by others previously.<sup>10</sup> Figure 1a,b shows scanning electron microscope (SEM) images of the METS used for the measurements of suspended and supported graphene, respectively. The METS consists of a 300 nm thick SiN<sub>x</sub> layer as mechanical support and 60 nm thick Pt metallization on top for electrical connection. The heater and sensor labeled in Figure 1a each comprises a Pt loop as a resistance thermometer suspended by six long beams for thermal isolation from the bulk substrate. To facilitate transfer and patterning of extremely fragile graphene, the nominally suspended heater and sensor structures are not released until the graphene has been finally placed and

\* To whom correspondence should be addressed. E-mail: (B.L.) phyllibw@nus.edu.sg; (J.T.L.T.) elettl@nus.edu.sg.

<sup>⊥</sup> These authors contributed equally to this work.

Received for review: 8/18/2010

Published on Web: 12/13/2010

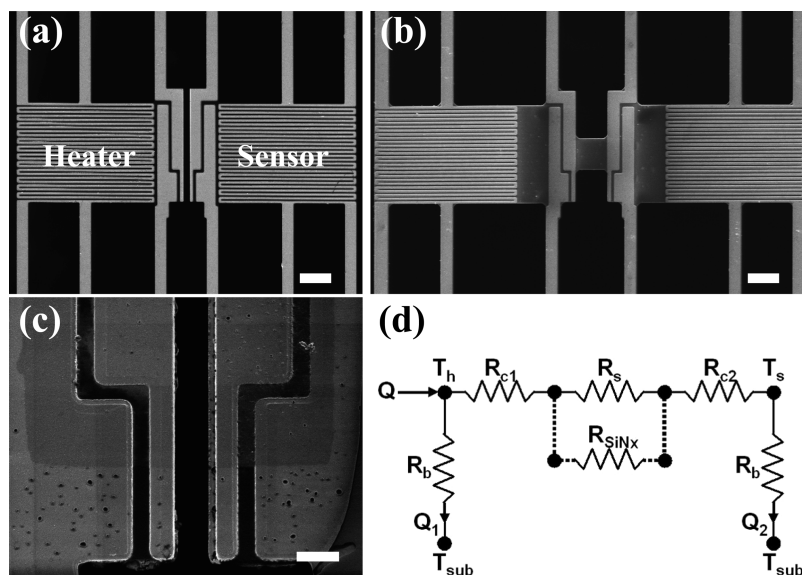


FIGURE 1. (a,b) SEM images of the METS for suspended and supported graphene samples; scale bar: 5  $\mu\text{m}$ . (c) SEM image of suspended sample S4; scale bar: 1  $\mu\text{m}$ . (d) Equivalent thermal circuit of the device,  $R_{\text{SiNx}}$  is the thermal resistance of the nitride platform for supported samples.

sized. FLG flakes were mechanically exfoliated on an oxidized Si substrate with 285 nm thick  $\text{SiO}_2$  and located under an optical microscope. A 600 nm thick polymethyl-methacrylate (PMMA) layer was spin-coated on top and baked at 120  $^\circ\text{C}$  in an oven for 30 min to improve its adhesion with the graphene. After immersion in a 45 wt % KOH solution at room temperature for about 2 h, the PMMA membrane detached from the substrate and was transferred onto the METS. The FLG flake on the underside of the PMMA was clearly visible under an optical microscope and was aligned to the test structure by moving the PMMA membrane with micromanipulated probes. Because of the hydrophobic nature of the PMMA, the FLG adhered very well to the METS after natural drying in air. The 600 nm thick PMMA was readily used as a resist layer for electron beam lithography (EBL) patterning and acted as a protective mask when the FLG was etched into a rectangular shape using oxygen plasma. For supported flakes, an additional Cr/Au (5/100 nm) layer was deposited on top of the FLG to improve its thermal contact with the heater and sensor, while the active region of the FLG is defined by the spacing between the metallization on the two sides. After lifting-off the PMMA in acetone, the METS with the aligned FLG flake was released and suspended by selective removal of the underlying Si substrate in a dry etcher for suspended samples or in a 45 wt % KOH solution for supported samples. The sample was thermally annealed at 600 K in vacuum ( $4 \times 10^{-7}$  mBar) for 12 h to remove any possible contamination from the PMMA residue.

We fabricated four FLG samples (S1–S3, 3-layer; S4, 5-layer), all patterned to have the same width ( $W$ ) of 5.0  $\mu\text{m}$ . Samples S1–S3 are supported by  $\text{SiN}_x$  with a length ( $L$ ) of 5.0, 2.0, and 1.0  $\mu\text{m}$ , respectively, while S4 is suspended

with a length of 1.0  $\mu\text{m}$ . Figure 1c shows the SEM image of S4 taken after all the measurements had been carried out.

We followed the method described by Shi et al.<sup>10</sup> for the thermal measurements. A direct current  $I_h$  was passed through the heater loop for the heating. The four-terminal electrical resistance of the Pt loops  $R_h$  and  $R_s$  were acquired using lock-in amplifiers by passing a very small alternating current (500 nA, 2017 Hz for the heater, and 1917 Hz for the sensor) that superimposes on  $I_h$ . The heater and sensor temperatures ( $T_h$  and  $T_s$ ) were then obtained based on  $R_h$  and  $R_s$  that had been calibrated against the substrate temperature of the METS ( $T_{\text{sub}}$ ) which sits on a PID-controlled heater stage with a sensitivity of 0.01 K. Others had previously assumed that the heater and sensor platforms have a uniform temperature distribution.<sup>10</sup> However from finite element method (FEM) modeling results as shown in Figure 2, the temperature change at the electrodes in contact with the sample was determined to be  $\sim 3.5\%$  higher (sensor) or  $\sim 2.0\text{--}4.0\%$  lower (heater), depending on the sample thermal conductance, than that measured by the sensor (heater) resistance thermometers. This systematic error in  $T_h$  and  $T_s$  was compensated for in all subsequent calculations. The Seebeck coefficient  $S$  was then calculated as  $S = -\Delta V/(T_h - T_s)$  where  $\Delta V$  is the potential difference between the central two electrodes measured by a multimeter (Hewlett-Packard 3458A). Figure 3a shows the  $S$ – $T$  curve for sample S1, which has a room temperature value of 18.0  $\mu\text{V/K}$ , suggesting that the FLG is slightly doped p-type. We have calculated the room temperature Seebeck coefficient for 3-layer graphene based on a density functional theory (DFT) model with the CASTEP package,<sup>11</sup> using the method described by Ni et al.<sup>12</sup> and Markussen et al.<sup>13</sup> The simulation results are plotted in Figure 3b, from which the extracted hole concentration  $p$

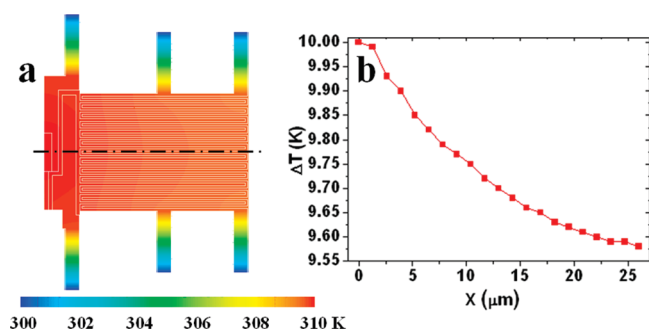


FIGURE 2. (a) Finite element method simulation of the temperature distribution on the sensor platform for a 10 K temperature rise on the left-hand-side electrode. The sensor membrane is  $25\ \mu\text{m} \times 15\ \mu\text{m}$ . Each of the six supporting beams of the actual device is  $400\ \mu\text{m}$  long and  $1.5\ \mu\text{m}$  wide. In the model, the beam length was scaled down to  $8\ \mu\text{m}$  with the thermal resistance of the beams kept the same by rescaling the thermal conductivity of the beams. (b) Temperature profile along the dash-dotted line in (a).

is  $\sim 4.7 \times 10^{11}\ \text{cm}^{-2}$ . From  $\mu = \sigma/pe$  with  $\sigma$  being the electrical conductivity (shown in Figure 3a) and  $e$  the elementary charge, the calculated room temperature hole mobility  $\mu$  has a high value of  $\sim 7000\ \text{cm}^2\ \text{V}^{-1}\ \text{s}^{-1}$ , indicating excellent sample quality.

Based on the equivalent thermal circuit shown in Figure 1d, the thermal conductance  $G$  of a suspended graphene sample is given by

$$G = G_b \frac{\Delta T_s}{\Delta T_h - \Delta T_s} = \frac{1.114 I_h^2 R_h \Delta T_s}{\Delta T_h^2 - \Delta T_s^2} \quad (1)$$

where  $\Delta T_{h,s} = T_{h,s} - T_{\text{sub}}$  and  $G_b = 1/R_b = [I_h^2(R_h + R_L)]/(\Delta T_h + \Delta T_s) = (1.114 I_h^2 R_h)/(\Delta T_h + \Delta T_s)^{10}$  is the thermal conductance of the six  $\text{SiN}_x$  beams connected to the heater. Here  $R_L$  is the electrical resistance of each of the two connecting beams passing the heating current  $I_h$  and is  $\sim 11.4\%$  of  $R_h$ . The correction factor 1.114 is used to account for the heating contribution from these two beams. The small heat capacity of the heater and sensor that results in fast temperature settling time allows rapid data acquisition with an accompanying measurement sensitivity of  $T_h$  and  $T_s$  of 0.03 K, translating into a sensitivity of  $\sim 10^{-10}\ \text{W/K}$  in the calcula-

tion of  $G$ . The thermal conductance of supported samples was extracted using a method similar to that described by Seol et al.,<sup>9</sup> where the contribution of the  $\text{SiN}_x$  platform to the heat conduction was measured after removing the graphene using oxygen plasma. Subtracting this from the total value leaves the thermal conductance attributable to the graphene.

Typically, the temperature rise of the heater  $\Delta T_h$  and the sensor  $\Delta T_s$  shows a smooth quadratic increase when the heating current  $I_h$  ramps from 0 to  $50\ \mu\text{A}$  (Figure 4a) as expected from their linear relationship with the heating power  $Q = I_h^2(R_h + R_L)$ . The proportional relationship in the  $\Delta T_h - \Delta T_s$  plot shown in the inset indicates that  $G$  stays almost constant when the temperature change is small ( $\Delta T_h < 10\ \text{K}$ ). On the basis of  $\kappa = (GL)/(Wt)$  where  $t$  is the thickness of graphene, S1 shows a room temperature  $\kappa$  of  $1250\ \text{Wm}^{-1}\ \text{K}^{-1}$  (Figure 4b), which is comparable to that of pyrolytic graphite (PG).<sup>14</sup> The similarity to the bulk value is reasonable since the lateral dimensions of S1 are relatively large ( $5.0\ \mu\text{m} \times 5.0\ \mu\text{m}$ ). To investigate the effect of lateral confinement on  $\kappa$ , the lengths of S2 and S3 were patterned to be 2.0 and  $1.0\ \mu\text{m}$ , respectively, while keeping other parameters identical to those of S1. As shown in Figure 4c, the  $\kappa$  of S2 is remarkably lower than that of S1 with a room temperature value of  $327\ \text{Wm}^{-1}\ \text{K}^{-1}$ , and S3 has an even lower  $\kappa$  of only  $150\ \text{Wm}^{-1}\ \text{K}^{-1}$ . These  $\kappa$  values are underestimated due to the thermal resistances at the contacts between graphene and the electrodes, which will be discussed later in this paper. This effect is more significant for shorter samples, and contributes to the decreasing trend of  $\kappa$  from S1 to S3. In addition, for smaller graphene flakes, the phonon mean-free path (MFP) is restricted by the physical size ( $L$ ) and places a lower bound on the frequency of phonons in the thermal transport. In other words, acoustic phonons with longer wavelength are only available for heat transfer in larger graphene flakes. The inverse relationship of  $\kappa$  and the graphene size we have obtained is also consistent with theoretical calculations,<sup>15–17</sup> which predict a drastic reduction in  $\kappa$  as the graphene size drops below  $5\ \mu\text{m}$ .

The presence of a substrate is believed to impede the thermal transport in graphene due to scattering at the

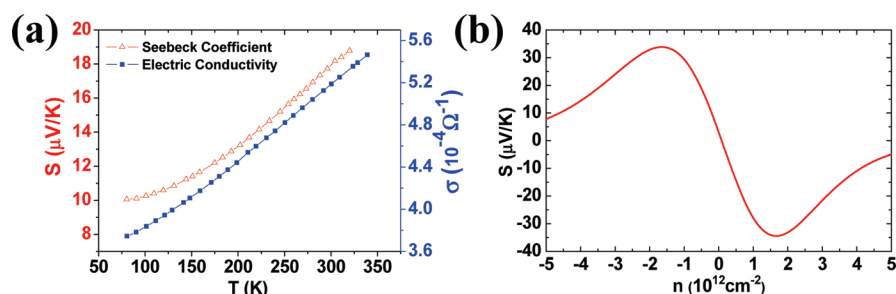


FIGURE 3. (a) Seebeck coefficient (red triangle) and four-terminal electrical conductivity (blue square) of S1 measured as a function of temperature. (b) Simulated Seebeck coefficient at 300 K as a function of carrier concentration for 3-layer graphene.

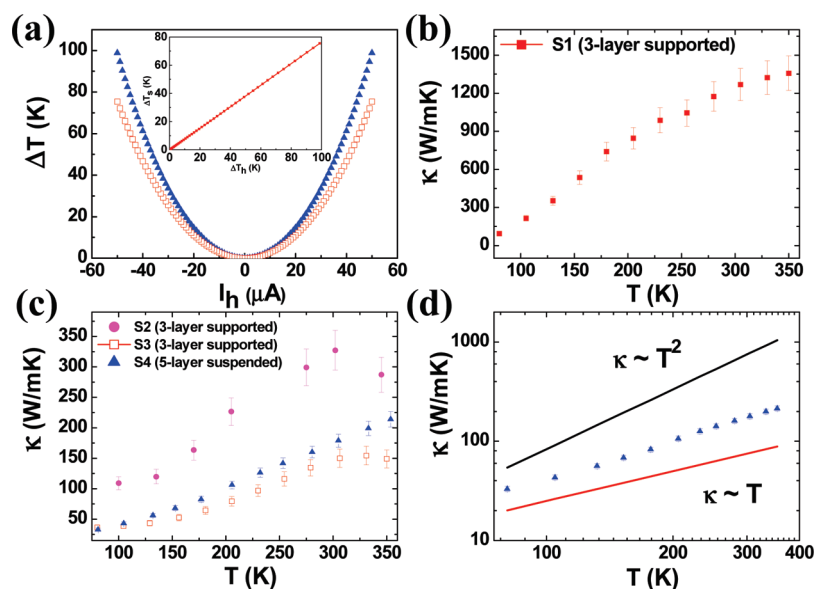


FIGURE 4. (a) Typical temperature rise in the heater ( $\Delta T_h$ , blue triangle) and the sensor ( $\Delta T_s$ , red square) as a function of the heating current  $I_h$  at  $T_{sub} = 300$  K. Inset:  $\Delta T_h$  vs  $\Delta T_s$ . (b, c) Measured thermal conductivity of S1–S4 as a function of temperature. (d)  $\kappa$  of S4 replotted on a logarithmic scale.

interface. In our experiment, S4 is suspended with the same lateral dimension as S3. Although  $\kappa$  is expected to be lower for thicker graphene due to the interlayer interactions,<sup>8</sup> the  $\kappa$  of the 5-layer S4 is actually higher than that of the 3-layer S3 with a room temperature value of  $170 \text{ W m}^{-1} \text{ K}^{-1}$  as shown in Figure 4c. It has been calculated that the  $\kappa$  value of SLG is lowered by up to 77 % at room temperature due to strong scattering of the phonon flexural (ZA) modes at the graphene-substrate interface.<sup>9</sup> However, the difference is only  $\sim 10\%$  in our case possibly because the upper layers of the FLG have less interaction with the substrate. The measured room temperature  $\kappa$  of the 3-layer S1 ( $1250 \text{ W m}^{-1} \text{ K}^{-1}$ ) is also higher than that reported for supported SLG ( $600 \text{ W m}^{-1} \text{ K}^{-1}$ ),<sup>9</sup> showing the diminishing effect of the substrate on the thermal transport in the top layers, and it is consistent with a recent report on thermal conductivity measurements of encased graphene.<sup>18</sup>

The  $\kappa$  of S1–S3 shows an increase with temperature and reaches a maximum at around 310–360 K. This  $\kappa$ – $T$  relation agrees well with that obtained for a supported SLG,<sup>9</sup> where the phonon transport is believed to be dominated by substrate interaction and umklapp scattering before and after the peak, respectively. However, for the suspended sample S4,  $\kappa$  keeps increasing and shows no sign of saturation even at 350 K. The turnover temperature is much higher than the 140 K measured for bulk PG<sup>14</sup> due to the restrictions on the phonon mean free path from the graphene edges. Boundary scattering is believed to dominate umklapp scattering over the temperature range of measurements. This temperature dependence of  $\kappa$  is also consistent with those obtained in the theoretical studies for small-sized graphene flakes<sup>15,19</sup> with dominant boundary effects. The  $\kappa$ – $T$  relation of S4 replotted on a logarithmic scale (Figure 4d) shows  $\kappa \sim$

$T^\alpha$  with  $\alpha = 1.4 \pm 0.1$ . This suggests that the flexural ZA phonon modes with a quadratic dispersion (giving  $\alpha = 1.5$ ) may contribute more significantly than the linearly dispersed in-plane LA and TA modes (giving  $\alpha = 2$ ).<sup>20</sup> This temperature dependence could also be caused by other factors. However, because of the limitation of our testing equipment, we could not go to very low temperatures to explore the exact mechanism. The measured values of  $\kappa$  are generally lower than those from theoretical studies, and we attribute the deviation to the presence of the graphene-contact interface, which constitutes a significant scattering site and is experimentally found to contribute a substantial thermal boundary resistance (TBR).

As shown in Figure 5, as heat transfers from the heater (A) to graphene (C) and from graphene to the sensor (E), the phonon transport is impeded at the contacts (B and D) due to sudden material and structural changes. In regions B and D, the cross-plane TBR between the Pt, graphene and  $\text{SiN}_x$  layers (normally referred to as “thermal contact resistance”) is negligible, since the contact area is large ( $5 \mu\text{m} \times 6 \mu\text{m}$ ) and the acoustic mismatch calculated from a half-space model<sup>21</sup> suggests a reflection coefficient of  $<1\%$  between the layers. It is also consistent with the low thermal contact resistance measured experimentally between graphene and  $\text{SiO}_2$ <sup>22</sup> or between graphite basal plane and Pt.<sup>23</sup>

The phonon transport from region B to C (or C to D) is normally overlooked in the thermal analysis of bulk materials, but becomes critical for low-dimensional samples. When heat is conducted by the graphene lattice vibration, the thermal waves are scattered at the B–C junction due to the different boundary conditions arising from the additional Pt layer in region B. At intermediate or high temperatures, transmission at the interface is mainly determined by the



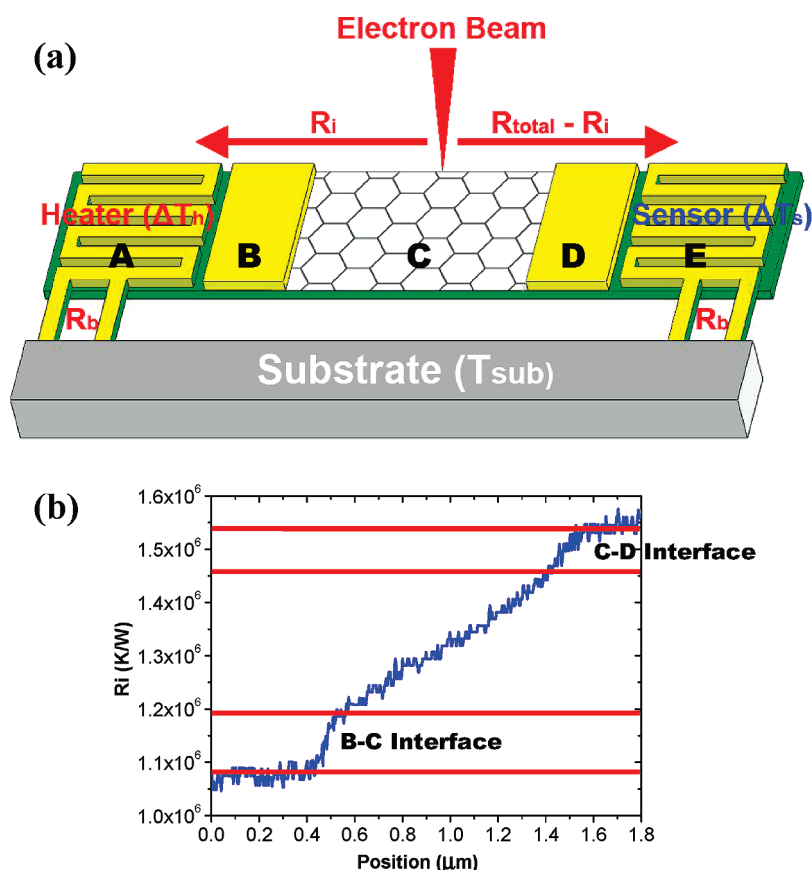


FIGURE 5. (a) Schematic of the localized electron beam heating technique. The connecting beams were only drawn on one side.  $R_b$ ,  $R_{\text{total}}$ , and  $R_i$  denote the thermal resistances of: the connecting beams, from heater to sensor, and from heater to electron beam spot respectively. (b) Spatially resolved thermal resistance  $R_i$  of sample S3.

mismatch in the density of phonon modes, since the phonon wavelength is short and the scattering is purely diffusive.<sup>24</sup> We have employed a noncontact electron beam heating method to quantitatively analyze the in-plane TBR incurred at this junction.

Instead of using Joule heating from the heater to establish a temperature gradient for thermal conductance measurement, a focused electron beam in an SEM was used to induce localized heating along the sample, while both the heater and sensor (in the previous configuration) acted as temperature sensors. As shown in Figure 5, the generated heat at the focused spot flows in both directions, and the relative heat fluxes are determined by the cumulative thermal resistance from the spot to the “heater” and to the “sensor”, respectively. By measuring  $\Delta T_h$  and  $\Delta T_s$ , the heat fluxes to the “heater” and “sensor” are  $\Delta T_h/R_b$  and  $\Delta T_s/R_b$ , respectively. The temperature rise at the focused spot is  $\Delta T_h + (\Delta T_h R_i)/R_b$  by considering the heat flux from the spot to the “heater”; or alternatively  $\Delta T_s + [\Delta T_s (R_{\text{total}} - R_i)]/R_b$  by considering the heat flux from the spot to the “sensor”, where  $R_{\text{total}}$  is the overall thermal resistance between the “heater” and “sensor”, and  $R_i$  is the cumulative thermal resistance from the electron beam heating position to the “heater”. It follows that  $R_i = R_b(a_0 - a_i)/(1 + a_i)$ , where  $a_0$  is the ratio of the

temperature rise  $\Delta T_{ho}/\Delta T_{so}$  when the electron beam is focused on the heater, and  $a_i$  is  $\Delta T_{hi}/\Delta T_{si}$  when electron beam is at position  $i$ . By scanning the focused electron beam along the structure and recording the corresponding  $a_i$ , the thermal resistance of the sample, the interface thermal resistance, as well as the contact thermal resistance as a function of the electron beam position can be spatially resolved.

$R_i$  for sample S3 is plotted in Figure 5 as the electron beam scans across regions B, C, and D. The value of  $R_i$  is constant in regions B and D showing good temperature uniformity and increases linearly in region C as expected. However, an abrupt step increase in the  $R_i$  value is observed at both B–C and C–D interfaces, which accounts for almost half of the total measured thermal resistance. The phenomenon could be more obvious in suspended graphene as the out-of-plane ZA phonons are employed for the thermal transport in addition to the LA and TA phonons in supported S3. Unfortunately, suspended graphene is too transparent to the electron beam for sufficient heat to be generated for the technique to work, and we are unable to verify this. Although this in-plane TBR is not part of the intrinsic characteristic of the thermal transport in graphene, it closely mimics the real-life scenario as there are always material or

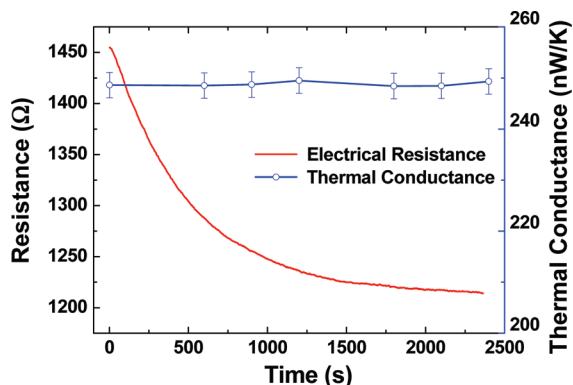


FIGURE 6. Resistance and thermal conductance change for S4 during  $N_2$  gas adsorption.

structural changes at the graphene edges when it is used as a thermal element in electronic devices.

Furthermore, we have also investigated the effects of surface adsorbates on the thermal transport of graphene. The pristine suspended S4 was exposed to a  $N_2$  atmosphere ( $1 \times 10^{-3}$  mBar) at room temperature. On the basis of the kinetic theory of gases, the mean free path of  $N_2$  molecules at  $1 \times 10^{-3}$  mBar is several centimeters, which is much greater than the separation between the heater and sensor. Hence the parasitic thermal conductance through the gas can be calculated using  $G_{h-s,N_2} = (CvA)/3$ ,<sup>10</sup> where  $C$  and  $v$  are the volumetric heat capacity and velocity of  $N_2$  molecules, respectively, and  $A$  is the equivalent area of the heater and sensor. The estimated  $G_{h-s,N_2} = 1.5 \times 10^{-10}$  W/K and is well below the thermal conductance of the sample ( $2.5 \times 10^{-7}$  W/K). Thus the parasitic thermal conductance has little effect on the results. As shown in Figure 6, when the  $N_2$  gas is physisorbed onto the graphene surface,  $R_G$  decreases due to doping effects and stays constant when the adsorption reaches saturation. However, the  $\kappa$  value shows negligible difference before and after  $N_2$  adsorption. A similar result was obtained when S4 was annealed again and exposed to an  $O_2$  atmosphere. Unlike the electrical properties, the thermal transport properties of graphene appear to be rather insensitive to gas adsorbates on its surface at room temperature. Thus for real-life devices operating under ambient conditions, the air molecules covering the graphene surface will not adversely affect its thermal conductivity.

In conclusion, we have experimentally studied the thermal conductivity of both suspended and supported few-layer graphene using a thermal-bridge configuration. The relatively larger supported sample S1 shows a room temperature  $\kappa$  of  $1250 \text{ W m}^{-1} \text{ K}^{-1}$ , comparable to that of bulk graphite. It is found that  $\kappa$  strongly depends on the size of graphene and is reduced by  $\sim 85\%$  when the sample length is reduced from  $5.0$  to  $1.0 \mu\text{m}$ . The influence of substrate is shown by the difference in  $\kappa$  of the suspended S4 and supported S3 with the same lateral dimensions, and the effect diminishes in the top layers away from the substrate. The  $\kappa$ - $T$  plot of S4 has a much higher turnover temperature than bulk

graphite due to the dominant boundary scattering for small-size flakes; and its  $\kappa$  increases with  $T$  following a power law with an exponent  $1.4 \pm 0.1$ , suggesting that the flexural phonon modes contribute significantly to the thermal transport of the suspended graphene. The measured values of  $\kappa$  are generally lower than those from theoretical studies possibly due the presence of the graphene-contact interface, which is shown to be a significant scattering site especially for smaller samples. In addition, the thermal transport of graphene is found to be insensitive to surface gas adsorbates, which is desirable for devices operating under ambient conditions. Detailed study on the length dependence of the thermal conductivity and the effects of interlayer interactions are underway and will be reported in future work.

**Acknowledgment.** We would like to thank Dr. Y. K. Koh for his comments on this manuscript. This work was supported in part by an NRF CRP Grant on Graphene related Materials & Devices and National University of Singapore research Grants R-263-000-494-646 and R-144-000-222-646.

## REFERENCES AND NOTES

- Geim, A. K.; Novoselov, K. S. *Nat. Mater.* **2007**, *6*, 183–191.
- Saito, K.; Nakamura, J.; Natori, A. *Phys. Rev. B* **2007**, *76*, 115409.
- Peres, N. M. R.; Lopes dos Santos, J. M. B.; Stauber, T. *Phys. Rev. B* **2007**, *76*, No. 073412.
- Jiang, J.-W.; Wang, J.-S.; Li, B. *Phys. Rev. B* **2009**, *79*, 205418.
- Balandin, A. A.; Ghosh, S.; Bao, W.; Calizo, I.; Teweldebrhan, D.; Miao, F.; Lau, C. N. *Nano Lett.* **2008**, *8*, 902–907.
- Faugeras, C.; Faugeras, B.; Orlita, M.; Potemski, M.; Nair, R. R.; Geim, A. K. *ACS Nano* **2010**, *4*, 1889–1892.
- Cai, W.; Moore, A. L.; Zhu, Y.; Li, X.; Chen, S.; Shi, L.; Ruoff, R. S. *Nano Lett.* **2010**, *10*, 1645–1651.
- Ghosh, S.; Bao, W.; Nika, D. L.; Subrina, S.; Pokatilov, E. P.; Lau, C. N.; Balandin, A. A. *Nat. Mater.* **2010**, *9*, 555–558.
- Seol, J. H.; Jo, I.; Moore, A. L.; Lindsay, L.; Aitken, Z. H.; Pettes, M. T.; Li, X.; Yao, Z.; Huang, R.; Broido, D.; Mingo, N.; Ruoff, R. S.; Shi, L. *Science* **2010**, *328*, 213–216.
- Shi, L.; Li, D.; Yu, C.; Jang, W.; Kim, D.; Yao, Z.; Kim, P.; Majumdar, A. *J. Heat Transf.* **2003**, *125*, 881–888.
- Clark, S. J.; Segall, M. D.; Pickard, C. J.; Hasnip, P. J.; Probert, M. I. J.; Refson, K.; Payne, M. C. *Z. Kristallogr.* **2005**, *220*, 567–570.
- Ni, X.; Liang, G.; Wang, J.-S.; Li, B. *Appl. Phys. Lett.* **2009**, *95*, 192114.
- Markussen, T.; Jauho, A.-P.; Brandbyge, M. *Phys. Rev. B* **2009**, *79*, No. 035415.
- Slack, G. A. *Phys. Rev.* **1962**, *127*, 694–701.
- Nika, D. L.; Ghosh, S.; Pokatilov, E. P.; Balandin, A. A. *Appl. Phys. Lett.* **2009**, *94*, 203103.
- Klemens, P. G. *J. Wide Bandgap Mater.* **2000**, *7*, 332–339.
- Klemens, P. G. *Int. J. Thermophys.* **2001**, *22*, 265–275.
- Jang, W.; Chen, Z.; Bao, W.; Lau, C. N.; Dames, C. *Nano Lett.* **2010**, *10*, 3909–3913.
- Lan, J.; Wang, J.-S.; Gan, C. K.; Chin, S. K. *Phys. Rev. B* **2009**, *79*, 115401.
- Mingo, N.; Broido, D. A. *Phys. Rev. Lett.* **2005**, *95*, No. 096105.
- Crocker, M. J. *Handbook of Acoustics*; John Wiley and Sons: New York, 1998.
- Chen, Z.; Jang, W.; Bao, W.; Lau, C. N.; Dames, C. *Appl. Phys. Lett.* **2009**, *95*, 161910.
- Prasher, R. *Phys. Rev. B* **2008**, *77*, No. 075424.
- Alvarez, F. X.; Alvarez-Quintana, J.; Jou, D.; Rodriguez Viejo, J. *J. Appl. Phys.* **2010**, *107*, No. 084303.